Nanoscale

Strong Interlayer Coupling Induced Charge Redistribution Forms Robust Non-Atomic Electron Scattering Sites in Bi_2Se_3/Transition Metal Dichalcogenide 2D Heterostructures

Journal:	*Nanoscale*
Manuscript ID	NR-ART-05-2019-004412.R1
Article Type:	Paper
Date Submitted by the Author:	20-Jul-2019

Complete List of Authors:	Hennighausen, Zachariah; Northeastern University, Physics Lane, Christopher; Northeastern University, Physics Buda, Ioana; Northeastern University, Physics Mathur, Vineet; Northeastern University, Physics Bansil, Arun; Northeastern University, Physics Kar, Swastik; Northeastern University, Physics

Strong Interlayer Coupling Induced Charge Redistribution Forms Robust Non-Atomic Electron Scattering Sites in Bi_2Se_3/Transition Metal Dichalcogenide 2D Heterostructures

Zachariah Hennighausen,[1] Christopher Lane[1], Gianina Buda[1], Vineet Mathur[1], Arun Bansil[1], and Swastik Kar[1,*]

[1]Department of Physics, Northeastern University, Boston, MA 02115

When 2D materials are vertically stacked, new physics emerges from interlayer orbital interactions and charge transfer modulated by the additional periodicity of interlayer atomic registry (moiré superlattice). Surprisingly, relatively little is known regarding the real-space distribution of the transferred charges within this framework. Here we provide the first experimental indications of a real-space, non-atomic lattice formed by interlayer coupling induced charge redistribution in vertically stacked Bi_2Se_3/Transition Metal Dichalcogenide (TMD) 2D heterostructures. Robust enough to scatter 200 keV electron beams, this non-atomic lattice generates selected area diffraction patterns that correspond excellently with simulated patterns from moiré superlattices of the parent crystals suggesting their location at sites of high interlayer atomic registry. Density functional theory (DFT) predicts concentrated charge pools reside in the interlayer region, located at sites of high nearest-neighbor atomic registry, suggesting the non-atomic lattices are standalone, reside in the interlayer region, and are purely electronic.

*Authors for correspondence, Email: hennighausen.z@husky.neu.edu; s.kar@northeastern.edu; ar.bansil@northeastern.edu

Keywords: 2D materials, heterostructures, interlayer coupling, interlayer interaction, density functional theory (DFT), TEM, SAED, transition metal dichalcogenides, bismuth selenide

Interlayer coupling can trigger a variety of phenomena in vertical 2D heterostructures, including creating new excitons (both interlayer and moiré),[1,2] modifying e-h recombination pathways,[3,4] altering Raman vibrational modes,[5] shifting the absorption profile,[6] enabling super-dense storage of lithium,[7] and inducing superconductivity.[8] In many instances, these new properties are strongly modulated by the formation of moiré superlattices, where the periodic variations of atomic registry between the two layers generate a new "lattice" with significantly modified band structure, electronic, optical and magnetic properties.[8–10] Since it is possible to artificially stack 2D layers with arbitrary twist angles, understanding and controlling the enhanced interactions at sites of high atomic registry in twisted 2D bilayers has become the central focus of research by many theoretical[11] and experimental efforts[12] in recent times. Dark-field TEM imaging,[10] high-resolution TEM imaging (Figure S10),[13] and STM[14,15] are able to visualize the moiré superlattices, but cannot independently probe the interlayer region or interlayer interaction because these measurements include the electrons' interaction with both parent layers as well.

In contrast, high-energy selected area electron diffraction (SAED) is able to probe the interlayer region of 2D materials, in part due to the small wavelength of the electrons (0.0251Å at 200 keV) and the low scattering angles inherent to SAED (~0.6°). The wavelength of the high-energy electrons are orders of magnitude smaller than the effective separation between the layers, which allows them to independently scatter from sites in the interlayer region, thereby greatly reducing the possibility of interference or multiple scattering features between the two parent crystals. Additionally, the very small scattering angles inherent to SAED, combined with the atomically thin nature of the samples, prevent strong reflections from the upper lattice becoming initial waves for the lower lattice. Hence, wave-interference and double diffraction effects present in multiple slit optical systems are very unlikely here (see Section S4 for amplifying discussion). Together, this indicates that the presence of moiré superlattice spots using SAED of 2D materials is due to the presence of non-atomic electron scattering sites, formed by interlayer coupling induced charge redistribution.

Nearly all past works on 2D moiré lattices apply a 2D fast Fourier transform (FFT) of real-space images as a means to simulate moiré "diffraction" patterns, rather than showing their real appearance in, e.g. a SAED measurement. Previous work showed that the lower scattering probability of the incoming high-energy electrons, combined with the generally weaker scattering cross section of non-atomic scattering sites, make identifying and measuring moiré superlattice SAED spots in vertically-stacked 2D graphene structures difficult.[16] In fact, we were able to find only one published work that demonstrates moiré superlattice spots using high-energy SAED, where the results suggest moiré superlattice spot brightness in bilayer graphene 2D structures is influenced by the twist angle and atomic registry.[10] Our work indicates that the strong interlayer coupling in vertically-stacked Bi_2Se_3/TMD 2D heterostructures induces significant charge redistribution, a surprising discovery considering both Bi_2Se_3 and TMD are considered to have "weak" van der Waals interlayer bonding. This is in contrast to layered graphene 2D structures which can have stronger π-π interlayer interactions, due to graphene's out-of-plane π orbitals.[17,18]

In this work we show direct observation of SAED patterns whose positions correspond to the moiré superlattices in 2D heterostructures, at room temperature. We argue that these are not from interference or multiple scattering features between the two parent crystals, nor from adsorption of foreign atoms (e.g., oxygen, bismuth, selenide), but rather from interlayer coupling induced charge redistribution into non-atomic scattering sites periodically spaced and oriented to match the moiré superlattice. Further, density functional theory (DFT) calculations predict that the interlayer coupling induces the formation of a purely-electronic charge lattice residing in the interlayer region which matches the orientation and size of the experimentally observed spots.

Of note, this work demonstrates the effect in *four* different Bi_2Se_3/TMD 2D heterostructures, including a TMD alloy (Bi_2Se_3/MoS_2, $Bi_2Se_3/MoSe_2$, Bi_2Se_3/WS_2, and $Bi_2Se_3/MoSe_{2-2x}S_{2x}$), and at multiple twist angles. To the best of our knowledge, no previous work has demonstrated this effect on so many different samples and at such high electron energies (200keV), suggesting that

the interlayer coupling induced charge redistribution is particularly robust in this family of 2D heterostructures. Previous work demonstrates that Bi_2Se_3/MoS_2 2D heterostructures have a strong interlayer coupling that quenches the signature photoluminescence of monolayer MoS_2 and modifies the Raman spectra.[3,4] Further, the interlayer coupling appears to facilitate the formation of a moiré superlattice with its own unique bandstructure (Figure S12), and modify the recombination energy of the exciton quasiparticles (Figure S11). A follow-up work found strong interlayer couplings in the other 2D heterostructures – $Bi_2Se_3/MoSe_2$, Bi_2Se_3/WS_2, and $Bi_2Se_3/MoSe_{2-2x}S_{2x}$ – using various intensities of a focused electron beam to modify the structure.[19] Together, the body of literature suggests a strong interlayer coupling exists within this family of 2D heterostructures.

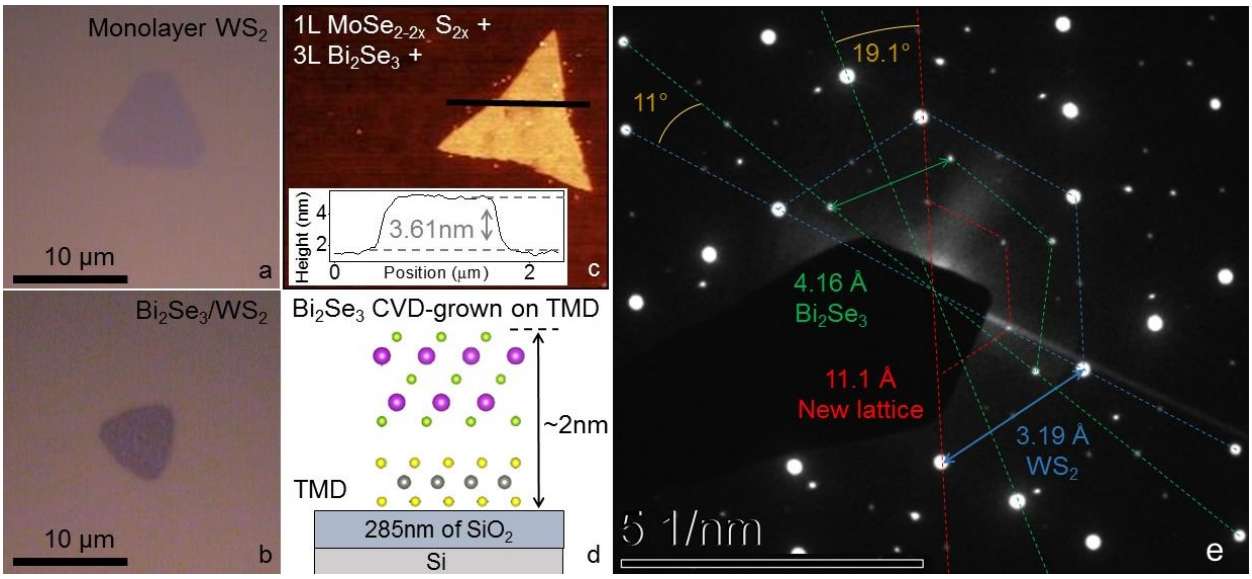

Figure 1: New lattice observed using high-energy selected area electron diffraction of vertically stacked Bi_2Se_3/TMD 2D heterostructures. (a) and (b) are optical images of monolayer WS_2 and a Bi_2Se_3/WS_2 2D heterostructure, respectively. A contrast is observed on the 2D heterostructure because Bi_2Se_3 grew monolayer with bilayer islands. (c) Atomic Force Microscope (AFM) scan showing three layers of Bi_2Se_3 grew evenly on monolayer $MoSe_{2-2x}S_{2x}$, an alloy of MoS_2 and $MoSe_2$. (d) Diagram representing the four different 2D heterostructures studied in this paper: Bi_2Se_3 grown on $MoSe_2$, MoS_2, WS_2, and $MoSe_{2-2x}S_{2x}$. The TMD is grown on SiO_2, and then Bi_2Se_3 is grown on top of the TMD. (e) Selected area electron diffraction (SAED) image of a Bi_2Se_3/WS_2 2D heterostructure with the in-plane lattice parameters labeled. Lattice parameters were calculated by measuring the spot separation. The distinct dots (labelled in blue and green) indicate the TMD and Bi_2Se_3, respectively, both grow highly crystalline. A third, new set of diffraction spots (red label) is present that has no known atomic basis and follows the geometric moiré superlattice pattern of the 2D heterostructure. As discussed later, moiré patterns only manifest when lattices are effectively multiplied, suggesting the strong interlayer coupling induces significant charge redistribution into periodic electron scattering sites, robust enough to scatter

Figure 1a shows an optical image of monolayer WS_2 grown on SiO_2 using vapor-phase chalcogenization.[20] Bi_2Se_3 samples were then grown on top of such WS_2 flakes using vapor-phase deposition. Figure 1b shows a Bi_2Se_3/WS_2 2D heterostructure with 1-2 layers of Bi_2Se_3 grown on monolayer WS_2. Figure 1c is an atomic force microscope (AFM) scan of a $Bi_2Se_3/MoSe_{2-2x}S_{2x}$ 2D heterostructure. Interestingly, three layers of Bi_2Se_3 grew on the monolayer TMD, while none grew on the SiO_2, suggesting the TMD substrate stabilizes the Bi_2Se_3 in its few layer morphology and is a preferred surface over the SiO_2. AFM measurements suggest all the 2D heterostructures contained between 1-3 layers of Bi_2Se_3 on top of a monolayer TMD. Figure 1d schematically shows how the two different materials stack up on the substrate. Figure 1e is a high energy SAED image of a Bi_2Se_3/WS_2 2D heterostructure with the diffraction patterns (with a six-fold symmetry) corresponding to the two parent crystals Bi_2Se_3 and WS_2 as labeled along with their corresponding lattice parameters. In addition, a third set of spots (also with a six-fold symmetry) labeled "New lattice" can be clearly seen with smaller reciprocal lattice dimensions (and hence much larger real-space dimensions), which has the same lattice structure, size, and orientation as the moiré superlattice of the parent crystals, and which we attribute to interlayer coupling induced charge redistribution into periodically spaced scattering sites. Before discussing the justifications for such an assignment, relevant details about SAED are described below that are necessary to understand our major claims.

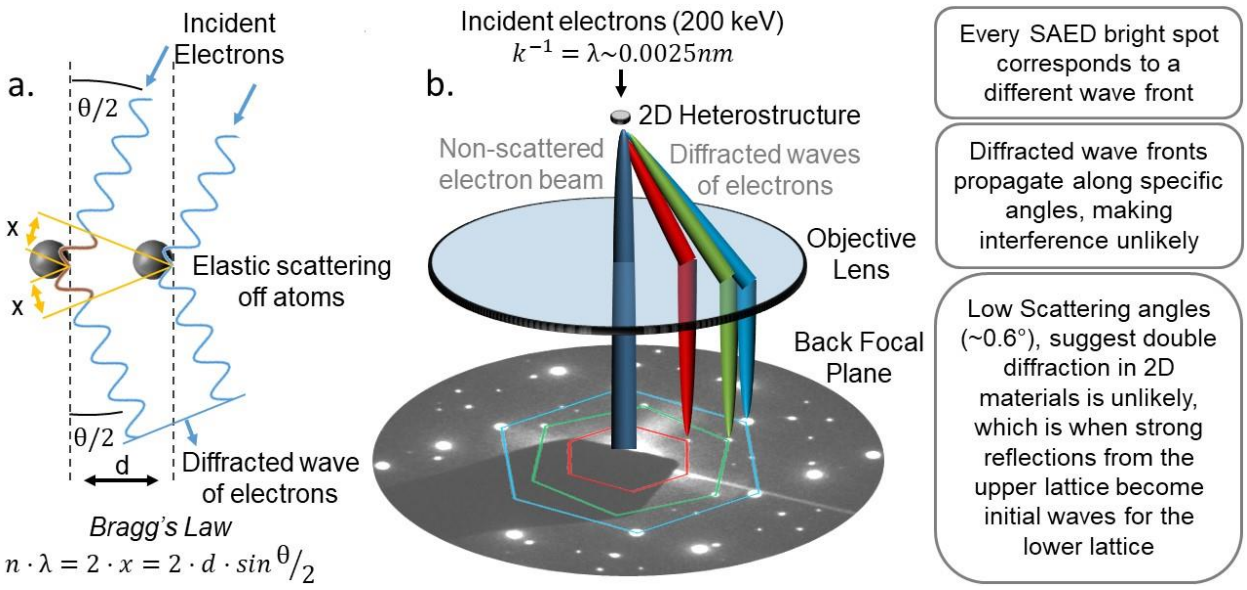

Figure 2: Simplified descriptions of pertinent SAED concepts. (a) Scattering mechanism for high-energy SAED follows Bragg's law, where electrons incident at a non-zero angle elastically scatter from atoms. In the diagram shown, the left electron must travel a longer distance (i.e., 2·x) for a diffracted wave front to form. In sharp contrast to multi-slit diffraction optical setups, the electrons must both elastically scatter and be incident at a non-zero angle for diffraction to occur. (b) Simplified diagram of a TEM in SAED mode, and important observations. As per Bragg's law, each lattice diffracts at a different angle because their lattice spacing's are different. As explained in Section S4, it is unlikely that wave-interference or double diffraction are able to produce moiré superlattice spots in high-energy SAED, suggesting such spots are from new scattering sites, which we attribute to the purely electronic crystal residing in the interlayer region.

Figure 2 shows simplified descriptions of pertinent SAED concepts. Figure 2a illustrates the scattering and diffraction mechanism involved in SAED, and the corresponding Bragg's law equation.[21] Electrons incident at non-zero angles are elastically scattered from the atoms, where one electron must travel a longer distance (i.e., 2·x). If the Bragg's law is satisfied, then a wave front forms. Figure 2b shows a simplified description of SAED using the SAED in Figure 1e, along with important observations on the right side. Note that each crystal diffracts a wave front at a different angle related to its lattice constant. In sharp contrast to multi-slit diffraction optical setups, neither wave-interference nor double diffraction are likely to produce moiré superlattice spots in high-energy SAED as explained further in Section S4. This is in agreement with high-energy SAED measurements of twisted bilayer MoS_2 2D structures, where moiré superlattice spots could not be detected, suggesting their emergence in Bi_2Se_3/TMD 2D heterostructures is due to the formation of a unique electronic lattice (Figure S10).[22]

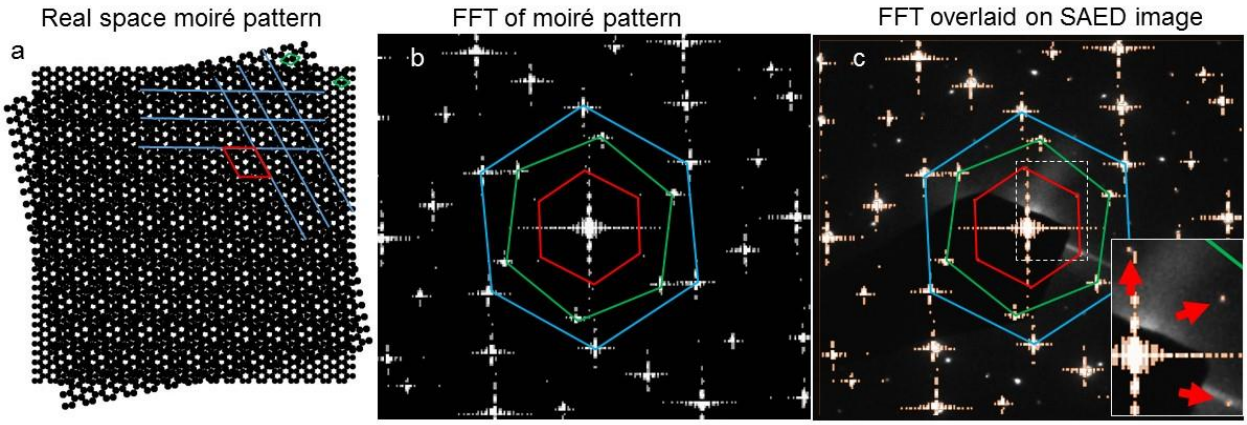

d

	Lattice ratio	Moiré lattice parameter (Å)	Angle: WS_2 to Bi_2Se_3 (deg)	Angle: Moiré to Bi_2Se_3 (deg)
Commensurate unit cell	1.309	11.06	10.89°	19.1°
Modeling	1.31	11.1	10.9°	19.1°
Experiment	1.31±0.02	11.1±0.12	10.9°±0.2°	19.1°±0.2°

Figure 3: Electronic moiré superlattice scattering sites formed by the interlayer coupling. (a) Simplified real-space model of the 2D heterostructure in Figure 1e. Two lattices with in-plane lattice parameters representing the WS_2 and Bi_2Se_3 crystals were twisted and then overlaid, thereby collapsing both lattices into the same 2D plane, over-writing pixels, and inducing the emergence of a moiré pattern (see methods section and section SI.1). Moiré patterns only manifest when there is an effective multiplication between two lattices. The moiré pattern lattice spacing and unit cell are identified by the blue and red lines, respectively. (b) 2D Fourier transform of the same model, thereby converting it to wavelength space to show the periodicities present, with the lattices labeled, where the blue, green, and red hexagons correspond to the WS_2, Bi_2Se_3, and moiré superlattice, respectively. (c) 2D Fourier transform (orange shading) overlaid on the SAED image seen in Figure 1e (white spots), where the near-perfect alignment of the spots suggests the model captures the system sufficiently. Interestingly, the moiré superlattice spots match the experimental new lattice spots, suggesting the new lattice forms congruently with sites of high atomic registry in the moiré superlattices of Bi_2Se_3 and WS_2. The inset with red arrows indicate patterns from the new lattice that are hidden under the red hexagon in the main image due to overlap of the modeling and experimental spots. (d) Table with the parameters from the mathematically calculated commensurate unit cell (see SI for more info), the model, and the experimentally measured values. All the values are nearly identical and well within the error, demonstrating close agreement between theory, modeling, and experiment. As discussed in the manuscript, optical diffraction theory or intuition should not be used to model or interpret high-energy SAED results, as the electron scattering and diffraction mechanisms are distinct from those in the optical case.

To begin with, the extra diffraction pattern could not be associated with any known atomic basis, but always have a real-space equivalent to the moiré superlattice structure of the 2D heterostructures being probed. This observation is demonstrated for a typical 2D heterostructure in Figure 1 (see also Section S3). First, to simulate the real-space superlattice, hexagonal lattices representing the TMD and Bi_2Se_3 layers scaled to experimentally measured lattice parameters and twist angles, were digitally generated, twisted, and then superimposed into a composite image. An example of such a simulated superlattice created (using the lattice

parameters and twist angle values from Figure 1e), is presented in Figure 3a, where the blue lines and the red rhombus have been used to visualize and measure the lattice spacing and unit cell of the clearly visible moiré superlattice. Next, a 2D FFT was performed on this superimposed image to show it in the wavelength space (reciprocal space) and identify the periodicities present, including the moiré superlattice (Figure 3b). Figure 3c shows an overlap of Figure 3b on to the actual SAED pattern shown earlier in Figure 1e. In all cases investigated, the 2D FFT-generated and experimentally-obtained bright spots are in near perfect alignment - including the new lattice - suggesting that the experimentally observed additional spots have a direct correlation with the structure of the moiré superlattice of the parent crystals. Although previous work successfully simulated SAED images of bilayer graphene structures using a 2D FFT of real-space configurations,[10,23] we do not claim our method fully captures the complex dynamics of SAED, but only serves to demonstrate that the new lattice spots match the moiré superlattice.

We note the digital superposition of the real-space simulated lattices flattens them into a single plane, and contains no layer-separation information in the perpendicular direction, which allows the 2D FFT to retain the superlattice-induced spots. In other words, the top-down view (along the z-axis) is how the SAED electrons would perceive the 2D heterostructure *if the two parent lattices were merged into the same plane*. Conceptually, this 2D FFT of the superimposed "2D heterostructure" displays the wavelength space and periodicities present.

The Diophantine equation shown in Section S1 was used to calculate the corresponding commensurate unit cell (Figure 3d), verifying that the SAED spots are in fact correlated to the moiré superlattice pattern, and not some other artifact.[24] And finally, the moiré lattice was absent when the TMD and Bi_2Se_3 lattices were individually Fourier transformed and overlaid (Section S2), demonstrating it is not an artifact from either lattice individually.

It is unlikely that the additional SAED spots simply result from interference or multiple scattering features between the two parent crystals. Mathematically, the formation of moiré patterns – or moiré effects – requires an interaction (or non-linear operation) between the two

parent lattices (see Section S1 for details).[24,25] For example, when images of periodic structures are overlaid, pixels are over-written as both images are collapsed onto the same surface. This over-writing of pixels, vice simply summing their intensities, reflects a non-linear "superposition" that produces a visual moiré pattern. In contrast, when 2D crystals are stacked, the different layers do not reside in the same plane, but are separated by ~ angstroms. The possibility of interferences between the two layers is hence remote, since the layer-center separation (~10Å) is massive (~400×) compared to the wavelength of the electrons (0.0251Å at 200 keV), suggesting the electrons perceive the two materials independently. Additionally, the combination of the very low scattering angles of high energy electrons in SAED (~0.6°), the atomically thin height (~2-4nm), and the large interlayer separation (~3.5Å) of the samples, indicates the multiple scattering features demonstrated in 3D heterostructures (e.g., double diffraction) and optical systems are unlikely (see Sections S4 and S5 from the SI).

It is important to mention that optical diffraction theory or intuition should not be used to model or interpret high-energy SAED results, as the electron scattering and diffraction mechanisms are distinct from those involved in the optical case.[26–28] For example, when modeling optical diffraction, no limits are placed on the angular distribution of scattered photons. In sharp contrast, high-energy SAED electrons only scatter at very low angles (0.6°), disallowing interference or double diffraction in 2D materials (see Section 4).[26–28] This is in agreement with previously published works that show multiple scattering, interference, and double-diffraction effects from high-energy electrons are highly improbable for samples of bilayer graphene placed on ~5nm of boron nitride, suggesting such effects are equally as improbable in our equivalently thin samples.[10,23]

Absorption or surface adsorption of foreign atoms (e.g., oxygen) is unlikely to produce the new moiré superlattice SAED spots. DFT calculations predict minimal charge redistribution at the surface with negligible changes to the energy landscape, suggesting energetically preferred states following the moiré superlattice are nonexistent. The intercalation of atoms is equally improbable as historically atomic intercalation diminishes the interlayer coupling, while all our

as-grown 2D heterostructures indicate strong interlayer couplings with quenched photoluminescence. In fact, previous work found the possible intercalation of oxygen in Bi_2Se_3/MoS_2 2D heterostructures diminished the interlayer coupling.[4] Additionally, the quartz tube is evacuated of gases prior to growth, and insufficient growth time exists for large bismuth and/or selenium atoms to intercalate. Lastly, the moiré superlattice SAED spots are a fraction of the intensity of the monolayer TMD spots (~1-6%), suggesting the new scattering sites have an equivalent reduction in scattering cross section. In contrast, a periodic arrangement of foreign atoms would be expected to yield much brighter spots, equivalent to the atoms in the 2D heterostructure. Although our study cannot completely rule out these scenarios, our analysis indicates they are unlikely.

Hence, we conclude that the observed new diffraction spots are not resulting from composite interferences of diffraction patterns from the atomic lattice of the parent crystals, or the introduction of foreign atoms, but are likely due to diffraction from a completely new lattice that is driven by the same underlying parameters that are involved in the generation of the moiré superlattice of the parent crystals. As discussed below, we believe most likely this new lattice resides in the interlayer region and is non-atomic, being entirely composed of charge redistribution.

These results raise three important questions: (1) What do the electronic moiré lattice scattering sites look like, (2) where do they reside, and (3) why does the lattice follow the moiré pattern, vice a different structure? We address these questions by performing first principles DFT calculations, which have been demonstrated to predict relatively accurate structural information and electronic charge distribution in solids.[29] Our DFT calculations (discussed later) predict the formation of a purely electronic 2D lattice residing in the interlayer region whose unit cell size and relative orientation are in agreement with the experimentally observed moiré pattern in our system, suggesting that such a purely electronic lattice may be responsible for the experimentally observed diffraction spots.

Although the DFT-predicted electronic lattice's dimensions are in complete agreement with experiment, further work is required to determine if the charge redistribution is sufficiently intense to scatter high-energy SAED electrons. Bloch-wave and multislice simulations[30], when combined with first-principles lattice calculations to accurately predict the charge distribution, have successfully modeled high-resolution TEM (HRTEM) and convergent-beam electron diffraction (CBED), demonstrating the sensitivity of electron scattering to charge redistributions, and underscoring the importance of using robust first principles results to predict the charge distribution (see Section 5).[31–34] Despite the success with HRTEM and CBED, we were unable to find any literature that simulated SAED images of lattices calculated using first-principles, including a highly-cited TEM simulation textbook,[34] possibly due to the difficulty in accurately modeling SAED scattering cross sections of charge pools and bonding. Sophisticated SAED simulation methods require previously measured or calculated atomic scattering factors,[28] and, to the best of our knowledge, no methods have been developed that accurately predict the scattering factor of bonding and charge pools. We did, however, find two published works which simulated SAED images of twisted bilayer graphene using a multiscale finite element method (FEM) that involved applying a 2D FFT to relaxed real-space configurations.[10,23] The success of this method suggests 2D FFTs can be used to simulate SAED images when applied correctly.

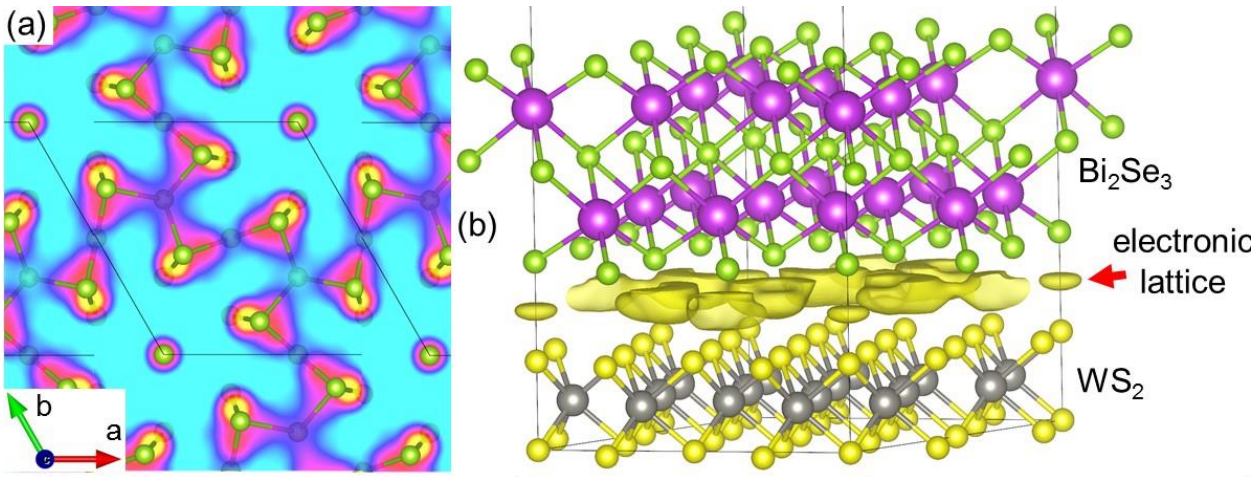

(c)

	In-plane Lattice parameter (Å)	Twist angle: Lattice to Bi_2Se_3 (deg)
High energy SAED observed new lattice	11.1±0.12	19.1°±0.2°
DFT predicted interlayer electronic lattice	11.1	19.1°

Figure 4: Charge pools form between nearest interlayer neighbors. (a) DFT calculated interlayer charge redistribution due to the interlayer coupling of a twisted 1L Bi_2Se_3 + 1L WS_2 2D heterostructure, using the lattice parameters described in Figure 3d. The image is a cut of the plane lying equidistant from both materials. The nearest neighbor atoms are included in the image. It can be seen that the charge redistribution is concentrated between nearest interlayer neighbors. (b) Cross-section view for the same DFT calculated 2D heterostructure, showing charge pools form between nearest neighbors. Since the atomic registry (or nearest neighbors) is determined by the moiré pattern, the charge pools form a purely electronic lattice that follows the moiré pattern. (c) Table with the parameters from the experimentally measured third-crystal and the DFT calculated interlayer electronic lattice, demonstrating their complete agreement. Together the experimental and theoretical work suggest that the high energy electrons might be scattering from the DFT-predicted interlayer charge pools.

Figure 4 shows DFT calculations for the predicted charge redistribution into the interlayer region due to the interlayer coupling in a 2D heterostructure (1-layer Bi_2Se_3 and 1-layer WS_2 twisted to 10.9° matching the structure shown in Figure 3c). DFT calculations for the other 2D heterostructures, along with the experimental data, are detailed in Section S3. Figure 4a is a charge density difference plot for a plane in the interlayer region equidistant from the Bi_2Se_3 and TMD layers, where red color denotes higher charge density. The charge congregates between nearest neighbor atoms (shown in the image), revealing possible bonding that forms between the layers. Figure 4b is a cross-section image of the same DFT calculation, showing both the Bi_2Se_3 and WS_2 layers, as well as the shape and relative displacement of the predicted interlayer charge pooling. The charge pools form a lattice with long-range order, where the unit cell size and twist angle (see Figure 4c) are in complete agreement with the experimentally observed new diffraction pattern in Figure 1e. The interlayer hybridization between nearest neighbor

atoms appears to be the primary mechanism for charge redistribution into a lattice that follows the moiré superlattice. Together these results provide strong evidence that the new set of spots seen in our heterostructures are likely a planar lattice of purely electronic charge pools that reside midway between the two parent crystals in the Bi_2Se_3/WS_2 2D heterostructure twisted to 10.9°.

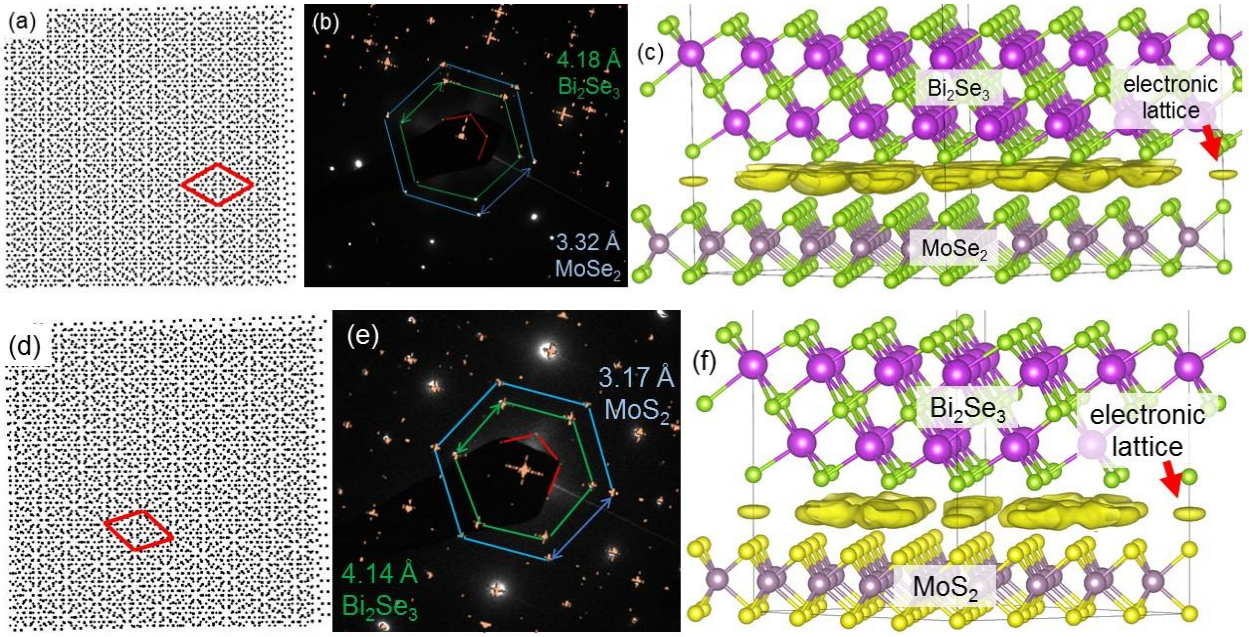

Figure 5: Interlayer coupling induced moiré superlattice scattering sites for $Bi_2Se_3/MoSe_2$ and Bi_2Se_3/MoS_2 2D heterostructures. (a) and (d) Simplified real-space models of $MoSe_2/Bi_2Se_3$ and MoS_2/Bi_2Se_3 2D heterostructures in (b) and (e), respectively. (b) and (e) 2D FFTs of the real-space models ((a) and (d), respectively) overlaid on high-energy SAED images, demonstrating the near-perfect fit between model and experiment. In (b) a portion of the 2D FFT is cropped away to reveal the SAED spots because the exceptionally close fit would otherwise cover the SAED spots completely. (c) and (f) DFT calculated 2D heterostructures with twist angles of 0°, vice 1.4° and 1.8°, respectively (see Section S3 for amplifying information). In agreement with Figure 4, DFT calculations predict that the interlayer coupling induces the formation of concentrated charge pools residing in the interlayer region between sites of high atomic registry. Together, the charge pools form an electronic lattice that precisely matches the moiré superlattice. The experimentally measured moiré superlattices are relatively large (31.6Å and 27.4 Å, respectively), and computationally too expensive to simulate using DFT. To overcome this, comparable 2D heterostructures were calculated with twist angles of 0°.

Figure 5 summarizes the experimental and theoretical results obtained for two different 2D heterostructures - $Bi_2Se_3/MoSe_2$ and Bi_2Se_3/MoS_2 – which are in agreement with the Bi_2Se_3/WS_2 results. Figure 5a and 5d show the simplified real-space models of the 2D heterostructures in Figures 5b and 5e, respectively. Figure 5b and 5e show 2D FFTs of the real-space models overlaid on the high-energy SAED images, where the close fit suggests the model captures the

system. Of note, the moiré pattern spots from the model match the new lattice spots, suggesting the new lattice is a product of the interlayer coupling between the parent crystals. Figure 5c and 5f are DFT calculations of $Bi_2Se_3/MoSe_2$ and Bi_2Se_3/MoS_2 2D heterostructures, respectively, with one Bi_2Se_3 and one TMD layer crystallographically aligned (i.e., 0° twist angle). The 2D heterostructures in Figures 5b and 5e have non-zero twist angles of 1.4° and 1.8°, respectively, thereby producing moiré superlattices too large to simulate using DFT. To overcome this, comparable crystallographically aligned 2D heterostructures were calculated.

For all 2D heterostructures, DFT calculations predicted the formation of an electronic lattice in the interlayer region, whose parameters (i.e., unit cell size and twist angle) are in complete agreement with the moiré patterns of the corresponding parent crystals (see section SI.3). Section S3 shows experimental and modeling data for $Bi_2Se_3/MoSe_{2-2x}S_{2x}$ 2D heterostructures at various twist angles, and a Bi_2Se_3/WS_2 2D heterostructure at 4.7°, where the experimental and modeling data are in agreement. The experimental observation of new SAED patterns that match perfectly with various DFT-predicted electronic lattices across multiple different 2D heterostructures and numerous twist angles, further supports our hypothesis, and suggests that the formation of a purely electronic 2D lattice (at least at certain twist angles) even at room temperature might be a characteristic trait of the investigated family of 2D heterostructures.

This naturally leads to the question whether the electronic lattice only exists at a discrete number of "magic" angles, or whether it exists at all twist-angles? Previous work demonstrated that Bi_2Se_3 grows at preferred twist-angles on monolayer TMDs, suggesting the interlayer coupling and electronic lattice intensity is angle dependent.[19] Although our work observed moiré superlattices at a variety of twist angles, we cannot rule out the possibility that only certain discrete angles facilitate an electronic lattice. Follow-up investigations are required to further illuminate why these dissimilar materials – a topological insulator and various TMDs – form such robust interlayer couplings. Previous work found topological surface states to only appear after seven quintuple layers, suggesting they are absent in our 2D heterostructures, which contained 1-3 quintuple layers of Bi_2Se_3.[35] We suspect that the interlayer electronic crystal

intensity can be modulated by hydrostatically pressing the layers together, a technique shown to increase the interlayer coupling.[36]

In conclusion, high-energy SAED measurements are reported on four different Bi_2Se_3/TMD 2D heterostructures (Bi_2Se_3/MoS_2, $Bi_2Se_3/MoSe_2$, Bi_2Se_3/WS_2, and $Bi_2Se_3/MoSe_{2-2x}S_{2x}$), and at numerous twist angles, where a new lattice with no atomic basis was detected. This new lattice corresponds to the moiré superlattice, suggesting the interlayer coupling redistributes charge, inducing the formation of robust electron scattering sites. This is surprising because it is traditionally assumed that such high energy (200 keV) SAED should only be able to reveal atomic structural information, owing to the large scattering cross sections (or factors) of atoms,[26–28] but are not sensitive to bonding or weak charge distributions. DFT calculations predict significant charge redistribution into concentrated pools residing in the interlayer region that form a purely electronic 2D charge lattice which follows the moiré superlattice. Together the results suggest strong interactions at sites of high atomic registry in Bi_2Se_3/TMD 2D heterostructures might be enabling charges to overcome the interlayer separation, thereby forming a purely electronic lattice situated between the two parent crystals. To the best of our knowledge, this is the first demonstration of SAED at such high electron energies being used to reveal non-atomic electronic scattering sites, and evidence of a purely electronic lattice at the interface of 2D materials. Very likely, the formation of interlayer charge pools between nearest interlayer neighbors plays an important role in the interlayer hybridization and coupling in these systems. Our findings provide significant new insights into how 2D layers interact, and how access to the 2D electronic lattice could open up opportunities for exploring physical properties of novel, purely-electronic periodic systems devoid of any atoms or defects. Control of such systems will very likely lead to new developments in nanoelectronics and optoelectronics, as well as other applications that depend on interfaces between 2D layers. [37–40]

Acknowledgement

Support for this research was received from the National Science Foundation, through grant number NSF ECCS 1351424, a Northeastern University Provost's Tier-1 Seed Grant, and the U.S. Department of Veterans Affairs, through the Post-9/11 GI Bill. The theoretical work at Northeastern University was supported by the US Department of Energy (DOE), Office of Science, Basic Energy Sciences grant number DE-FG02-07ER46352 (core research), and benefited from Northeastern University's Advanced Scientific Computation Center (ASCC), the NERSC supercomputing center through DOE grant number DE-AC02-05CH11231, and support (testing the efficacy of advanced functionals in complex materials) from the DOE EFRC: Center for Complex Materials from First Principles (CCM) under DE-SC0012575.

Conflict of Interest Statement: The authors declare that Northeastern University owns the IP around certain inventions on these materials, which are currently under process. At the time of submission, the authors did not perceive any competing financial interest.

Methods

Growth of TMD and TMD-alloy 2D crystals

All 2D TMDs, as well as the 2D TMD-alloy, were grown using vapor-phase chalcogenization (VPC).[20] The growth setup consisted of quartz tubes [1 inch (2.54 cm) in diameter] in a horizontal tube furnace (Lindberg/Blue M). A quartz boat, containing a thin layer of either MoO_2 or WO_2 powder (3 mg or 15mg, respectively) with SiO_2/Si (MTI Corporation) substrates suspended over the powder with the growth side facing down, was placed in the hot center of the furnace. Either Sulfur, selenium, or both powders (150 mg or 50mg, respectively) were used, depending on the material being grown. To grow the alloy $MoSe_{2-2x}S_{2x}$, both powders were used at the same time. Sulfur was placed near the insulating edge of the furnace upstream, whereas selenium was placed ~1cm past the insulating edge of the furnace upstream. The setup was pumped down and purged with argon gas before it was filled with an Ar atmosphere. Downstream was then opened to atmosphere, in addition to a constant 200 standard cubic centimeter per minute (SCCM) Ar flow. The furnace was heated to different temperatures and

at variable rates, depending on the material being grown. The growth was conducted in two stages, 1st-stage and 2nd-stage, where 2nd stage would start once the 1st-stage temperature was reached. See the below table for material specific growth information. After the elapsed time, the furnace was opened and allowed to cool rapidly.

2D Crystal	1st Rate (°C/min.)	1st Temp. (°C)	2nd Rate (°C/min.)	2nd Temp. (°C)	Hold time (min.)
MoS_2	50	500	5	712	20
$MoSe_2$	50	200	20	740	10
WS_2	50	1080	5	1150	25
$MoSe_{2(1-x)}S_{2x}$	50	100	30	750	10

Bi_2Se_3 growth was performed in a nearly identical vapor-phase deposition setup, except a heating wrap was coiled around the quartz tube at the down-stream end, leaving no gap between the furnace and the heating wrap. The Bi_2Se_3 powder (50 mg) was placed in the hot center of the furnace. The 2D TMD or 2D TMD-alloy substrate was placed downstream ~0.75cm from the boundary between the furnace and the heating wrap. The system was pumped down to a base pressure of ~10 mtorr before a 35-SCCM Ar flow was introduced, raising the growth pressure to ~490 mtorr. The heating wrap was set to a temperature of 245°C, and a temperature controller (J-KEM Scientific Model Apollo) ensured it remained within ±2°C. The furnace was heated at a rate of 50°C/min to 530°C and then held there for 20-25 min depending on the desired thickness. Once growth was completed, the furnace was opened and the temperature controller was de-energized, allowing the setup to cool rapidly.

Instrumentation

Raman and PL spectra were measured using a Renishaw Raman microscope equipped with a 488nm laser and a grating of 1800 lines/mm. A ×100 or ×150 objective focused the laser to diffraction-limited spot size. TEM images and SAED patterns were collected from a JEOL 2010F operated at 200 kV. AFM images were taken from a NanoMagnetics Instruments Ambient AFM. All Raman, PL, AFM, and UV-Vis experiments were performed under ambient condition.

Electron Beam Treatment (EBT) Studies

Prior to select area electron diffraction (SAED), the 2D heterostructures needed to be transferred to a transmission electron microscope (TEM) grid. The TEM grids used were Pelco QUANTFOIL® Holey Carbon film. PMMA C4 was first spin-coated at 4000 rpm for 60 s on the SiO_2 wafer with the 2D heterostructures and baked 180 C for 1:30 min. Then the chip was immersed in 1 M KOH solution for 4 hours. Obtained PMMA and heterostructure film transferred to new substrate. This was followed by acetone and IPA cleaning to remove PMMA residues. An optical picture 2D heterostructures transferred onto the TEM grid are below.

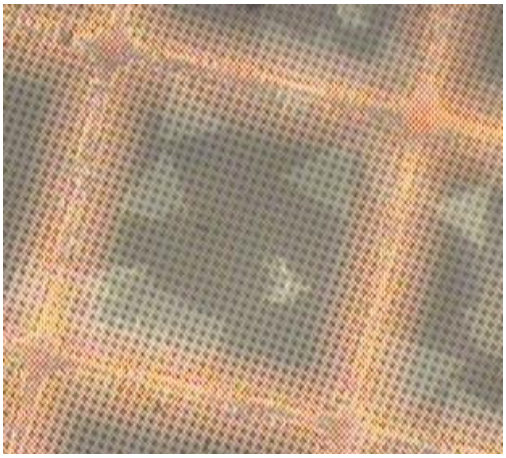

Optical Picture of Bi_2Se_3 2D heterostructures transferred onto a TEM grid

Once the grid was inside the TEM, a heterostructure suspended over a hole was found, zoomed-in, and then focused. Then the 200nm-diameter aperture was inserted and TEM was switched to SAED mode. Then the brightness was decreased to the lowest value, and an SAED image was taken.

Computational Methods

The ab initio calculations were performed using the pseudopotential projected augmented wave method [41] implemented in the Vienna ab initio simulation package [42,43] with an energy cutoff of 420 eV for the plane-wave basis set. Exchange-correlation effects were treated using the generalized gradient approximation (GGA),[44] and van der Waals corrections were included using the DFT-D2 method of Grimme,[45] where a 7 × 7 × 1 Γ-centered k-point mesh was used to

sample the Brillouin zone. A large enough vacuum of 15 Å in the z direction was used to ensure negligible interaction between the periodic images of the films. All the structures were relaxed using a conjugate gradient algorithm with an atomic force tolerance of 0.05 eV/Å and a total energy tolerance of 10^{-4} eV. The spin-orbit coupling effects were included in a self-consistent manner.

References

1. Ross, J. S. *et al.* Interlayer Exciton Optoelectronics in a 2D Heterostructure p–n Junction. *Nano Lett.* **17**, 638–643 (2017).
2. Zhang, N. *et al.* Moiré Intralayer Excitons in a MoSe2/MoS2 Heterostructure. *Nano Lett.* **18**, 7651–7657 (2018).
3. Vargas, A. *et al.* Tunable and laser-reconfigurable 2D heterocrystals obtained by epitaxial stacking of crystallographically incommensurate Bi2Se3 and MoS2 atomic layers. *Sci. Adv.* **3**, e1601741 (2017).
4. Hennighausen, Z. *et al.* Oxygen-Induced In-Situ Manipulation of the Interlayer Coupling and Exciton Recombination in Bi2Se3/MoS2 2D Heterostructures. *ACS Appl. Mater. Interfaces* (2019). doi:10.1021/acsami.9b02929
5. Ding, L. *et al.* Understanding Interlayer Coupling in TMD-hBN Heterostructure by Raman Spectroscopy. *IEEE Trans. Electron Devices* 1–9 (2018). doi:10.1109/TED.2018.2847230
6. Yuan, L. *et al.* Photocarrier generation from interlayer charge-transfer transitions in WS2-graphene heterostructures. *Sci. Adv.* **4**, e1700324 (2018).
7. Kühne, M. *et al.* Reversible superdense ordering of lithium between two graphene sheets. *Nature* **564**, 234 (2018).
8. Cao, Y. *et al.* Unconventional superconductivity in magic-angle graphene superlattices. *Nature* **556**, 43–50 (2018).
9. Dean, C. R. *et al.* Hofstadter's butterfly and the fractal quantum Hall effect in moire superlattices. *Nature* **497**, 598–602 (2013).

10. Yoo, H. *et al.* Atomic and electronic reconstruction at the van der Waals interface in twisted bilayer graphene. *Nat. Mater.* 1 (2019). doi:10.1038/s41563-019-0346-z
11. Tong, Q., Liu, F., Xiao, J. & Yao, W. Skyrmions in the Moiré of van der Waals 2D Magnets. *Nano Lett.* **18**, 7194–7199 (2018).
12. Yu, H., Liu, G.-B., Tang, J., Xu, X. & Yao, W. Moiré excitons: From programmable quantum emitter arrays to spin-orbit–coupled artificial lattices. *Sci. Adv.* **3**, e1701696 (2017).
13. Xu, S. *et al.* van der Waals Epitaxial Growth of Atomically Thin Bi2Se3 and Thickness-Dependent Topological Phase Transition. *Nano Lett.* **15**, 2645–2651 (2015).
14. Zhang, C. *et al.* Interlayer couplings, Moiré patterns, and 2D electronic superlattices in MoS2/WSe2 hetero-bilayers. *Sci. Adv.* **3**, e1601459 (2017).
15. Trainer, D. J. *et al.* Moiré superlattices and 2D electronic properties of graphite/MoS 2 heterostructures. *J. Phys. Chem. Solids* (2017). doi:10.1016/j.jpcs.2017.10.034
16. Latychevskaia, T., Escher, C. & Fink, H.-W. Moiré structures in twisted bilayer graphene studied by transmission electron microscopy. *Ultramicroscopy* **197**, 46–52 (2019).
17. Berashevich, J. & Chakraborty, T. Interlayer repulsion and decoupling effects in stacked turbostratic graphene flakes. *Phys. Rev. B* **84**, 033403 (2011).
18. Berashevich, J. & Chakraborty, T. On the Nature of Interlayer Interactions in a System of Two Graphene Fragments. *J. Phys. Chem. C* **115**, 24666–24673 (2011).
19. Hennighausen, Z. & Kar, S. Probing the Interlayer Interaction between Dissimilar 2D Heterostructures by In-Situ Rearrangement of their Interface. *2D Mater.* (2019). doi:10.1088/2053-1583/ab136e

20. Bilgin, I. *et al.* Chemical Vapor Deposition Synthesized Atomically Thin Molybdenum Disulfide with Optoelectronic-Grade Crystalline Quality. *ACS Nano* **9**, 8822–8832 (2015).
21. Thomas, J. & Gemming, T. *Analytical Transmission Electron Microscopy: An Introduction for Operators*. (Springer Netherlands, 2014).
22. Waduge, P. *et al.* Direct and Scalable Deposition of Atomically Thin Low-Noise MoS2 Membranes on Apertures. *ACS Nano* **9**, 7352–7359 (2015).
23. Zhang, K. & Tadmor, E. B. Structural and electron diffraction scaling of twisted graphene bilayers. *J. Mech. Phys. Solids* **112**, 225–238 (2018).
24. Zeller, P., Ma, X. & Günther, S. Indexing moiré patterns of metal-supported graphene and related systems: strategies and pitfalls. *New J. Phys.* **19**, 013015 (2017).
25. Lebanon, G. & Bruckstein, A. M. Variational approach to moiré pattern synthesis. *JOSA A* **18**, 1371–1382 (2001).
26. Bendersky, L. A. & Gayle, F. W. Electron Diffraction Using Transmission Electron Microscopy. *J. Res. Natl. Inst. Stand. Technol.* **106**, 997–1012 (2001).
27. *Transmission Electron Microscopy: Diffraction, Imaging, and Spectrometry*. (Springer International Publishing, 2016).
28. Spence, J. High energy electron diffraction and microscopy. By L. M. Peng, S. L. Dudarev and M. J. Whelan. Pp. 544. Oxford University Press, 2003. Price GBP 69.95. ISBN 0-19-850074-2. *Acta Crystallogr. A* **60**, 355–355 (2004).
29. Buda, I. G. *et al.* Characterization of Thin Film Materials using SCAN meta-GGA, an Accurate Nonempirical Density Functional. *Sci. Rep.* **7**, 44766 (2017).

30. Cowley, J. M. & Moodie, A. F. The scattering of electrons by atoms and crystals. I. A new theoretical approach. *Acta Crystallogr.* **10**, 609–619 (1957).
31. Ciston, J., Kim, J. S., Haigh, S. J., Kirkland, A. I. & Marks, L. D. Optimized conditions for imaging the effects of bonding charge density in electron microscopy. *Ultramicroscopy* **111**, 901–911 (2011).
32. Meyer, J. C. *et al.* Experimental analysis of charge redistribution due to chemical bonding by high-resolution transmission electron microscopy. *Nat. Mater.* **10**, 209–215 (2011).
33. Susi, T. *et al.* Efficient first principles simulation of electron scattering factors for transmission electron microscopy. *Ultramicroscopy* **197**, 16–22 (2019).
34. Kirkland, E. J. *Advanced Computing in Electron Microscopy*. (Springer US, 2010).
35. Bansil, A., Lin, H. & Das, T. Colloquium: Topological band theory. *Rev. Mod. Phys.* **88**, 021004 (2016).
36. Yankowitz, M. *et al.* Tuning superconductivity in twisted bilayer graphene. *Science* **363**, 1059–1064 (2019).
37. Ribeiro-Palau, R. *et al.* Twistable electronics with dynamically rotatable heterostructures. *Science* **361**, 690–693 (2018).
38. Wang, C. *et al.* Monolayer atomic crystal molecular superlattices. *Nature* **555**, 231–236 (2018).
39. Peng, L. *et al.* Effective Interlayer Engineering of Two-Dimensional VOPO4 Nanosheets via Controlled Organic Intercalation for Improving Alkali Ion Storage. *Nano Lett.* **17**, 6273–6279 (2017).
40. Song, T. *et al.* Giant tunneling magnetoresistance in spin-filter van der Waals heterostructures. *Science* eaar4851 (2018). doi:10.1126/science.aar4851

41. Kresse, G. & Joubert, D. From ultrasoft pseudopotentials to the projector augmented-wave method. *Phys. Rev. B* **59**, 1758–1775 (1999).

42. Kresse, G. & Furthmüller, J. Efficient iterative schemes for ab initio total-energy calculations using a plane-wave basis set. *Phys. Rev. B* **54**, 11169–11186 (1996).

43. Kresse, G. & Hafner, J. Ab initio molecular dynamics for open-shell transition metals. *Phys. Rev. B* **48**, 13115–13118 (1993).

44. Perdew, J. P., Burke, K. & Ernzerhof, M. Generalized Gradient Approximation Made Simple. *Phys. Rev. Lett.* **77**, 3865–3868 (1996).

45. Grimme, S. Semiempirical GGA-type density functional constructed with a long-range dispersion correction. *J. Comput. Chem.* **27**, 1787–1799 (2006).